AJNR

MR detection of hyperacute parenchymal hemorrhage of the brain.

S W Atlas and K R Thulborn

AJNR Am J Neuroradiol 1998, 19 (8) 1471-1477
http://www.ajnr.org/content/19/8/1471

AJNR Am J Neuroradiol 19:1471–1507, September 1998

MR Detection of Hyperacute Parenchymal Hemorrhage of the Brain

Scott W. Atlas and Keith R. Thulborn

BACKGROUND AND PURPOSE: **The detection of hemorrhage in acutely ill patients is crucial to clinical management. The MR features that allow diagnosis of intracerebral hematomas of less than 24 hours' duration are described and the mechanistic basis of these features is investigated.**

METHODS: **The clinical MR features of seven confirmed hyperacute intracerebral hematomas were compared with those of experimentally induced hematomas in a rat model in which detailed analyses of iron metabolism and morphometry were performed.**

RESULTS: **In all patients and all animals, a hypointense rim on T2-weighted spin-echo images that was less marked on T1-weighted spin-echo images was seen surrounding a central isointense or heterogeneous region of hyperacute hematoma. Histologically, the clot showed interdigitation of intact erythrocytes and tissue at the hematoma-tissue interface without significant hemosiderin, ferritin, or phagocytic activity. Biochemically, the iron from the extravasated blood was present only as heme proteins within the first 24 hours.**

CONCLUSION: **The hypointense rim on T2-weighted images, and to a lesser extent on T1-weighted images, is a distinctive feature of hyperacute hematoma. This pattern is consistent with magnetic susceptibility variations of paramagnetic deoxygenated hemoglobin within intact erythrocytes at a microscopically irregular tissue-clot interface. The detection of hemorrhage is important in the management of patients with acute stroke.**

The original and now generally accepted model for the appearance of intracerebral hematomas on MR images attributes the characteristic signal intensity patterns in evolving hemorrhage (1) to the products of iron metabolism and the integrity of the red blood cell. That model attributes the hypointense signal characteristics of acute hematomas seen in the first few days after hemorrhage on long–repetition time (TR)/long–echo time (TE) spin-echo images at 1.5 T to spin dephasing from water diffusing through magnetic field gradients generated by the magnetic susceptibility differences between diamagnetic tissue and paramagnetic deoxyhemoglobin confined within erythrocytes. Others have suggested that clot formation, clot retraction (2), and intracellular protein concentration (3) may play some role in generating the characteristic signal intensity pattern of acute intracranial hemorrhage.

Despite the fact that the appearance and progression of evolving intracranial hemorrhage on MR images have received extensive study over the past several years, the appearance in the immediate posthemorrhagic state, within the first few hours after bleeding, has rarely come to clinical attention. An early report of a series of older hematomas included an acute hematoma in the right putamen at 15 hours after the event (4). However, with the introduction of thrombolytic treatment and other interventions for hyperacute stroke, the question of identifying early stroke by MR imaging has immediate importance. Although CT is the usual means for detecting hemorrhage in this clinical setting, it is often not sensitive to ischemic insult in the first hours after symptom onset. The use of both CT and MR imaging is time-consuming and expensive. As diffusion and perfusion MR imaging are becoming integrated into the diagnosis of early stroke and into the monitoring of response to therapy, the role of MR imaging in detecting hemorrhage in patients with hyperacute stroke has assumed greater importance.

We report the MR appearance of hyperacute intracranial hematomas in seven patients imaged with a high magnetic field (1.5 T). To understand the mechanism underlying this appearance, a previously de-

Received November 20, 1997; accepted after revision April 6, 1998.

Supported by Public Health Service grant RO1 HL45176 and by General Electric Medical Systems.

From the Department of Radiology, Mount Sinai School of Medicine, New York (S.W.A.); and the MR Research Center, Department of Radiology, Presbyterian University Hospital, University of Pittsburgh Medical Center, Pittsburgh, PA (K.R.T.).

Address reprint requests to Keith R. Thulborn, MD, PhD, MR Research Center, Presbyterian University Hospital, 200 Lothrop St, Pittsburgh, PA 15213.

scribed rat model of cerebral hematoma was used to investigate the biochemical form and histologic distribution of iron during this hyperacute phase of hematoma (5). Such information was not available from the clinical cases, in which no invasive studies were possible. The animal model allowed the use of blood labeled with ^{59}Fe hemoglobin to follow quantitatively the biochemical pathway for the removal of iron from extravasated blood through heme proteins to storage products of ferritin and hemosiderin. Results for the biochemical forms of iron from hemoglobin over the first 24 hours are reported. These quantitative biochemical results are used to confirm the qualitative histopathologic results, in which stains for different iron products of hemoglobin breakdown (hemosiderin, Perls' Prussian blue stain; ferritin, immunochemical ferritin-specific stain) were used to determine the acute distribution of these substances in and around the lesions.

Methods

Eight patients (seven males and one female, ages 5 to 70 years) with proved early acute intracranial hematomas were examined with MR imaging. The diagnosis of early acute hematoma was proved in seven patients by CT studies performed without intravenous contrast administration. Surgical confirmation was obtained in three patients (including the sole patient without CT confirmation) within 24 hours after clinical presentation. All patients presented with either seizure or an acute change in neurologic status. All patients were imaged within the first 10 to 24 hours after ictus. MR imaging was performed as a part of standard clinical practice and the findings were assembled retrospectively into this report in compliance with the internal review boards of the authors' institutions

In seven patients, images were obtained using conventional spin-echo or fast spin-echo techniques at 1.5 T. Both short-TR/short-TE and long-TR/long-TE images were generated in each case. Short-TR/short-TE sequences had parameters of 600/11–20, whereas long-TR/long-TE sequences had parameters of 2500–3000/80. The long-TR dual-echo spin-echo sequence at 1.5 T had a short TE (= 30) and a long TE (= 80). Fast spin-echo images were obtained in more recent cases (acquisition parameters: 3600/84 with an echo train length of 8). In addition, six of the patients were imaged with a gradient-recalled echo sequence (multiplanar gradient-recalled acquisition in the steady state; acquisition parameters, 500–750/20–40 with a flip angle of 10–30°).

The rat model of cerebral hematoma was used as previously described and complied with the institutional guidelines for animal experimentation (5). The rats (n = 4) were imaged within 4 hours of hematoma formation on a 1.5-T whole-body imaging system using a dual-echo spin-echo sequence with a long TR (= 3000) and a first TE of 30 and a second TE of 80, a spin-echo sequence with a short TR (= 600) and a short TE (= 25), and a gradient-echo sequence with parameters of 250/11 and a pulse angle of 10°. The field-of-view was 16 cm, which was the smallest available. The section thickness was 3 mm. A 3-inch round surface coil was used to optimize the signal-to-noise ratio over the anesthetized rat, which was in a supine position over the coil.

After imaging, the rats were sacrificed by decapitation and the brains carefully removed into phosphate-buffered formalin for fixation (48 hours, 3°C). Thin-section (0.01-mm) frozen histologic sectioning was performed followed by standard staining techniques, including hematoxylin-eosin for morphology, Perls' Prussian blue for Fe(III) ions, and ferritin immunochemical staining for ferritin protein (5).

Parallel experiments to examine iron metabolism were performed with hematomas produced with iron (^{59}Fe) radiolabeled blood. Radiolabeled iron was incorporated into hemoglobin by weekly intraperitoneal injections of ^{59}Fe citrate (50–100 μCi) over 6 to 10 weeks. The specific activity (cpm/μg Fe) of the donor blood was determined in standard fashion by iron assay and gamma counting. Blood from these donor animals was used to produce hematomas in recipient animals (experimental group, n = 6) in identical fashion as for imaging. These animals were sacrificed by decapitation under general anesthesia between 1 and 24 hours after induction of the hematoma. The brains were removed immediately, divided into right and left hemispheres and cerebellum, rapidly weighed, and then frozen in liquid nitrogen. The right hemispheres were counted for ^{59}Fe iron activity, then subjected to homogenization, and then to 10 cycles of cold sonication, cold centrifugation, and resuspension in cold acetate buffer (1.0 mL, 100 mM, pH 4.5). This procedure ensured complete disruption of tissue and solubilization of all soluble iron proteins. The ^{59}Fe activities of the homogenate, washes, and residual pellet were determined, and the total iron content ascertained from the specific activity. The percentage of fractions of soluble and insoluble iron was calculated for the acetate buffer solubilization conditions.

The soluble fraction was characterized further by ion exchange carboxymethyl cellulose chromatography using a modification of a standard protocol described elsewhere for fractionation of soluble iron-containing proteins (6). The soluble fraction (0.2 mL) was loaded onto the columns in loading buffer (sodium citrate, 10 mM, pH 4.5, 8 mL) and eluted stepwise with the following buffers: sodium citrate (10 mM, pH 4.7, 8 mL), sodium citrate (50 mM, pH 5.5, 8 mL), sodium citrate (50 mM, 0.3 M NaCl, pH 5.7, 8 mL), and sodium hydroxide (0.1 M, 8 mL). Eluant fractions were counted for ^{59}Fe activity. Adequate separation of heme proteins and ferritin was verified using standard solutions of hemoglobin and ferritin eluted under identical conditions to those of the soluble brain fraction.

The insoluble fraction was characterized by solubility criteria using standard procedures for obtaining hemosiderin (7).

Results

Human Studies

All CT studies showed the typical imaging characteristics of acute hematomas: discrete high-attenuation mass lesions with low-attenuation edema in surrounding brain parenchyma.

The MR appearance of the hematomas was strikingly similar in all cases (Figs 1 to 3). On short-TR/short-TE T1-weighted images, the lesion was heterogeneous, nearly isointense with cortical gray matter (Figs 1A, 2A, and 3A), with a thin, slightly hypointense rim (Figs 1A, 2A, and 3A). Methemoglobin was not present, as indicated by the absence of hyperintensity on such images. The long-TR/long-TE T2-weighted images showed a heterogeneously hyperintense mass lesion (Figs 1B, 2B, and 3B) with a mild degree of perilesional high intensity, consistent with edema in adjacent brain, with or without an intervening region of fluidlike intensity between the hematoma and the edema (Figs 1B, 2B, and 3B). A thin rim of marked hypointensity and variable thickness was consistently identifiable on long-TR/long-TE images immediately surrounding the hematoma at its periphery, inside the region of fluidlike intensity (Figs 1B, 2B, and 3B). This rim of hypointensity was less easily

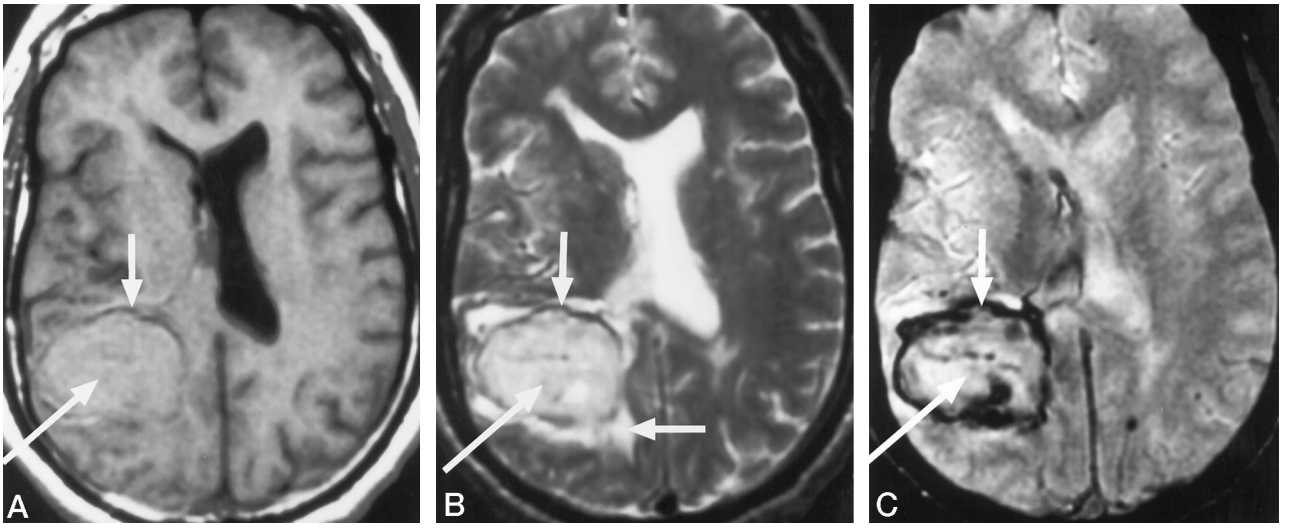

FIG 1. Case 1.
A, Axial short-TR/short-TE image (600/20/1).
B, Axial long-TR/long-TE image (3000/80/1).
C, Axial gradient-echo image (750/50/1; 10° flip angle).
The right temporoparietal lobe hematoma is isointense on the short-TR/short-TE image (*A, oblique arrow*) and shows heterogeneous hyperintensity on the long-TR/long-TE image (*B, oblique arrow*). On the long-TR/long-TE image, there is a rim of marked hypointensity surrounding the hematoma at this very early stage of hemorrhage (*B, vertical arrow*). The gradient-echo image (*C*) shows more marked signal loss around the lesion. Edema is present around the lesion on the long-TR/long-TE image (*B, horizontal arrow*).

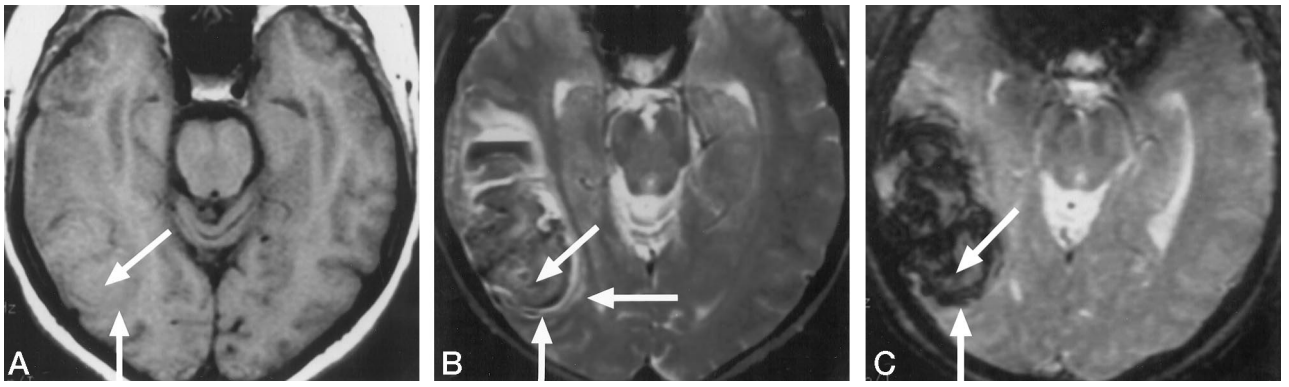

FIG 2. Case 2.
A, Axial short-TR/short-TE image (600/20/1).
B, Axial long-TR/long-TE image (2500/80/1).
C, Axial gradient-echo image (750/50/1; 10° flip angle).
The right temporal lobe hematoma is isointense on the short-TR/short-TE image (*A, oblique arrow*) and shows heterogeneous hyperintensity on the long-TR/long-TE image (*B, oblique arrow*). On the long-TR/long-TE image (*B, vertical arrow*), there is a rim of marked hypointensity surrounding the hematoma at this very early stage of hemorrhage. Edema is present around the lesion on the long-TR/long-TE image (*B, horizontal arrow*). The gradient-echo image (*C, oblique arrow*) shows marked signal loss throughout the bulk of the lesion. A debris-fluid level is present in a cavity in the anterior aspect of this lesion.

discernible on short-TR/short-TE images. The gradient-echo images showed more diffuse signal loss throughout the lesions with differences probably reflecting different times of imaging after the initial event (Figs 1C and 2C). These patterns were comparable to those reported for a hemorrhage at 15 hours after the event (4).

Animal Studies

Imaging.—Figure 4 shows representative long-TR/long-TE spin-echo images, long-TR/short-TE spin-echo images, short-TR/short-TE spin-echo images, and gradient-echo images of hematomas in the rat model at less than 4 hours after induction. These images revealed significant signal loss in the periphery of the lesion on the long-TR/long-TE images, the long-TR/short-TE images, and the short-TR/short-TE images. This hypointense boundary was more extensive than that observed on the clinical images, most likely reflecting the partial volume effects of a small lesion relative to the 3-mm-thick image in the rat model. The center of the lesion was isointense relative to the cortex. High signal surrounded the area of signal loss on the long-TR/long-TE images. No bright signal was present on the short-TR/short-TE images. On the gradient-echo images, signal loss occurred throughout the lesion.

FIG 3. Case 3.
A, Sagittal short-TR/short-TE image (600/20/1).
B, Long-TR/long-TE image (3000/80/1).
The left frontoparietal hematoma is isointense on the short-TR/short-TE image (*A, oblique arrow*) and hyperintense on the long-TR/long-TE image (*B, oblique arrow*), consistent with a diamagnetic mass. A peripheral rim of marked hypointensity surrounds the hematoma (*A* and *B, vertical arrow* and *small black arrows*). Perihematoma edema is seen outside the hypointense peripheral rim of the hematoma (*B, horizontal arrow*).

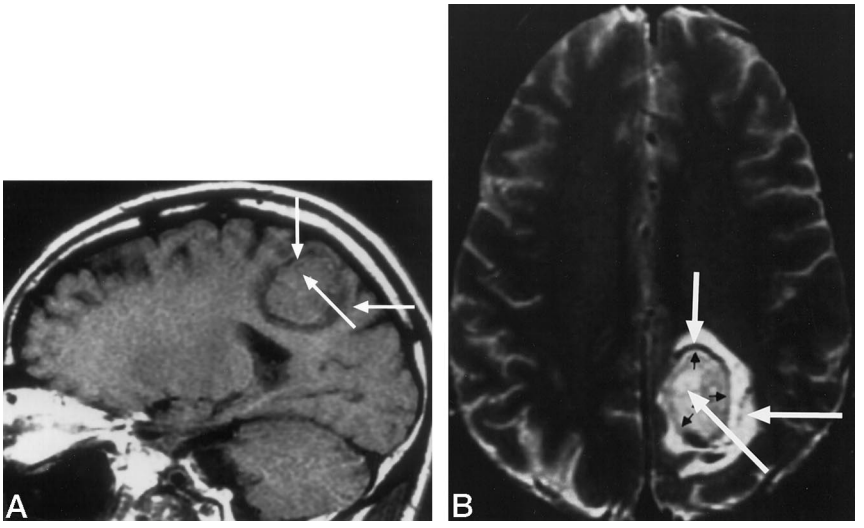

FIG 4. An experimentally induced hematoma in the anesthetized rat brain, imaged within 4 hours after induction.
A, Long-TR/short-TE image (3000/30/1).
B, Long-TR/long-TE image (3000/80/1).
C, Short-TR/short-TE image (600/25/1).
D, Gradient-echo image (250/11/1; 10° flip angle).
The intraparenchymal hematoma has an isointense central region (*long arrow*) with a hypointense rim (*short arrow*) on spin-echo images (*A, B,* and *C*), whereas the entire lesion is hypointense (*both arrows*) on the gradient-echo image (*D*).

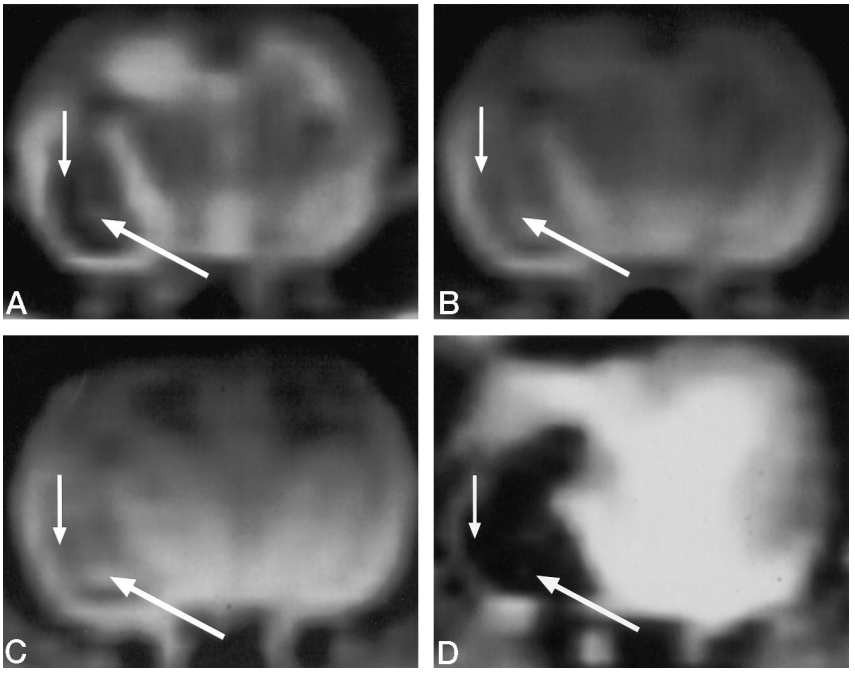

These signal characteristics mimic those of the clinical cases, making the model appropriate for more detailed invasive methods not possible in humans. The gradient in signal intensity from the inferior to superior aspect of the brain is attributable to the use of the surface coil for excitation and reception.

Histology.—The hematoma contained intact erythrocytes with little inflammatory repair response at this early stage. The clots, when preserved, showed uniform distribution of intact erythrocytes without retraction from the tissue-clot interface. Clot retraction was not identified explicitly, but since not all clot-tissue interfaces were preserved on every histologic preparation, those regions not preserved may have been areas of clot retraction. The boundary between hematoma and surrounding tissue showed interdigitation of erythrocytes and parenchymal tissue (Fig 5). The Perls' stain and ferritin immunochemical stain showed no evidence of staining in hematomas 1 day or younger in age. The histologic sections and MR images could not be compared directly owing to differences in thickness between the MR image (3 mm) and the histologic section (0.01 mm).

Biochemistry.—As no differences were found in the analyses of hematomas at 1 and 24 hours, the results were pooled for presentation. The iron injected as blood into the brains of living rats (n = 6) was separated into soluble (hemoglobin, methemoglobin, ferritin) and insoluble (hemosiderin, denatured protein) fractions. Essentially all the injected iron was in the soluble protein fraction for hyperacute hematomas, which was shown to be heme proteins (hemoglobin) by ion exchange chromatography. No indication of ferritin was found. The insoluble fraction was characterized by further solubility criteria as corresponding to denatured protein (being soluble in urea solutions) resulting from the initial homogenization procedure. No hemosiderin was present.

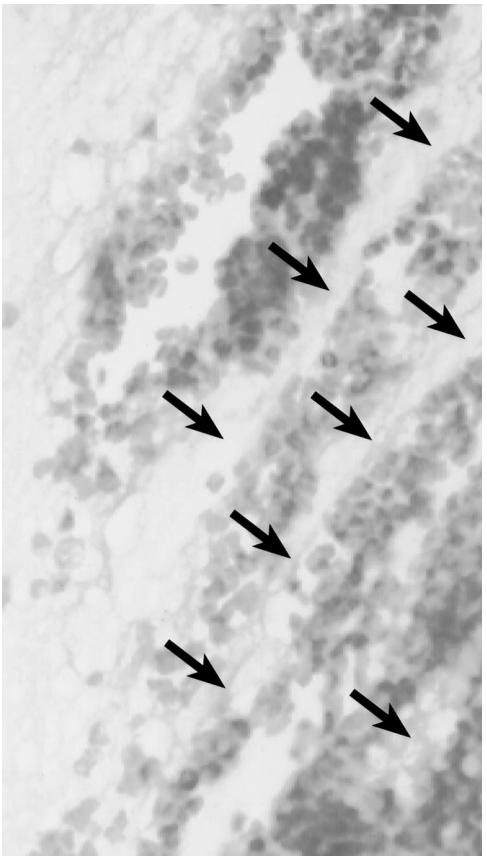

FIG 5. Histologic section of the tissue-clot interface of an experimentally induced hyperacute hematoma in rat brain shows interdigitation of blood clot and intact tissue (*arrows*). This interdigitation increases the tissue-clot surface area to promote deoxygenation of the clot periphery by the adjacent compressed tissue. The periodicity is such that water diffusion through the resultant magnetic susceptibility gradients results in MR signal loss.

Discussion

The identification of acute and hyperacute intracranial hemorrhage is critical to the determination of appropriate patient management, especially in the setting of stroke. Although few imaging studies have been obtained during the hyperacute event, owing to standard triage procedures, our experience indicates that this is changing. Hence, findings in this clinically important stage should be added to the model of the MR appearance of intracranial hemorrhage (8–10). The conceptual framework for understanding the MR appearance of cerebral hematoma has been summarized in numerous reviews (11–17) based on in vitro studies, animal models, and clinical observations (1, 4, 10, 11, 13, 18–28). The original model (1) emphasized the roles of iron associated with hemoglobin, edema, and gross structural changes in the hematoma in determining relaxation mechanisms underlying the variable MR patterns. Other pathophysiological processes, such as changes in integrity of the blood-brain barrier, nonparamagnetic protein concentration, and the presence of an underlying lesion, are also thought to contribute to signal intensity patterns on these images.

The rim of marked hypointensity seen in the hyperacute hematomas described above has been reported previously in studies using long-TR/long-TE MR sequences (4, 27, 28). The difference in magnetic susceptibility between hematoma and tissue was proposed on the basis of phase changes at the interface in a single hematoma at 15 hours (4). An in vitro investigation by Clark and colleagues (2) attempted to quantify the separate effects of deoxygenation, protein (hematocrit), clot formation, and clot retraction in generating signal intensity changes in acute clot. Their study indicated that the contributions of fibrin clot formation and clot retraction to T2 shortening were minimal (less than 2% combined). Further confirmation of the lack of significant relaxation enhancement in acute hemorrhage generated by protein macromolecules has been presented by others in studies of magnetization transfer (29). While there is still some controversy regarding the precise localization of the field gradients causing T2 effects in acute hematomas (18), magnetic susceptibility differences arising from intracellular deoxyhemoglobin are thought to represent the source of the signal loss during the acute phase (first several days) of intracranial hemorrhage.

Our results confirm the presence of a feature on MR images that allows clear identification of the earliest stage of intracranial hematoma; that is, the hyperacute hematoma. We believe that this initial stage represents a transition from a fully *oxygenated* hematoma to a fully *deoxygenated* hematoma, in which deoxygenation occurs initially at the periphery of the lesion. This peripheral deoxygenation generates T2-related signal loss that extends inward throughout the hematoma, as it is the low partial pressure of dissolved oxygen in the compressed underperfused surrounding tissue that provides the driving force for dissociation of molecular oxygen from hemoglobin. This mechanism is supported by the findings on gradient-echo images, in which signal loss occurs throughout the hematoma. The distinct rim of marked hypointensity at the periphery of the lesion on long-TR/long-TE images must reflect not just deoxygenation of hemoglobin in erythrocytes but also a property of the clot-tissue interface. A similar peripheral hypointense rim around hematomas as early as 3 hours after the event has also been reported using phase maps to demonstrate phase shifts in this region (30).

As intravoxel dephasing, not present on spin-echo images, sensitizes gradient-echo images to deoxygenation, these observations suggest that the tissue interface of the hematoma has properties that are different from the center of the clot.

The animal model allowed further analysis of the origin of these signal characteristics. The MR signal loss on long-TR/long-TE images (Fig 4A) and long-TR/short-TE images (Fig 4B) was greatest at the periphery and was seen even at the earliest time at which the animals were imaged (1 hour). The signal loss was also evident on the short-TR/short-TE images (Fig 4C), consistent with the frequently noted

hypointensity of very short T2 substances, even on "short"-TE images; that is, the TE is still long enough to allow the rapid T2-related relaxation to occur. As the TE was longer for the animals as compared with the human patients (25 milliseconds as compared with 11–20 milliseconds), this signal loss was more evident on the animal images. Differences in extent of peripheral signal loss from the clinical cases presumably reflect significant partial volume effects for such small lesions (2-mm diameter) and relatively low through-plane resolution (3 mm) in the animal model. No hyperintense signal was evident on short-TR/short-TE images (Fig 4C), excluding the presence of free iron or methemoglobin. The entire lesion was hypointense on gradient-echo images (Fig 4D) as seen in the human subjects (Figs 1C and 2C). Also, the rate of deoxygenation may be somewhat higher in rats, given their higher metabolic rate and the relatively greater mass effect with resultant underperfusion as compared with humans. The high signal on long-TR/long-TE images around the peripheral rim of hypointensity is consistent with either serum extravasated from the clot or edema in adjacent brain parenchyma. Since the peripheral rim of signal loss was associated with an enhanced transverse relaxation rate, clearly evidenced by the greater signal losses observed on the long-TR/long-TE spin-echo and gradient-echo images, mechanisms involving magnetic susceptibility–induced signal loss must be invoked.

The only paramagnetic source of significance in hemorrhage is iron from hemoglobin. Biochemically, this can be present as deoxy- (ferrous) or met- (ferric) heme proteins in erythrocytes or as iron (ferric) storage forms of ferritin and hemosiderin in phagocytes, such as glial cells and macrophages. The histologic and biochemical studies were used to distinguish between these sources of susceptibility effects.

We therefore propose that the peripheral rim of hypointensity in hematomas arises from rapid deoxygenation of hemoglobin within erythrocytes at the periphery of the lesion. Several factors may contribute to this effect. First, the surrounding tissue, compressed by the mass effect of the hematoma, is underperfused, and this oxygen deprivation leads to deoxygenation of adjacent blood. It is well documented that even as early as 1 minute after intracranial hemorrhage there is a decrease in cerebral blood flow as well as metabolic disturbance in the region surrounding the hematoma (31). Second, rapid acidification of this underperfused tissue causes the Bohr effect to promote local oxygen dissociation from hemoglobin. The interdigitation of clot and tissue generates a geometry of varying magnetic susceptibility that favors steep susceptibility-induced field gradients that are incompletely sampled by diffusing water protons. This diffusion through field gradients results in reduced signal as TE is extended and TR is long enough to avoid substantial T1 saturation effects. The pattern of signal changes suggests that deoxygenation occurs from the edge of the hematoma and progresses inwardly. As time evolves, severe deoxygenation extends throughout the hematoma, producing an MR appearance characteristically described for acute hematomas, the appearance of which is by far the most frequently encountered MR feature of early hemorrhage.

Conclusion

Our series of eight clinical cases extends the information provided in the previous isolated reports of hyperacute hemorrhage to suggest that the common pattern of a rim of hypointensity on long-TR/long-TE MR images is a characteristic transitional manifestation of early intracranial hematoma. We suggest that this feature of hyperacute hematoma, along with isointensity relative to white matter on short-TR/short-TE images and hypointensity on gradient-echo images, could be of practical use for detecting hemorrhage in stroke patients when diffusion-weighted MR imaging is being used to confirm the diagnosis of hyperacute stroke immediately before the initiation of therapy. The need for CT to detect hemorrhage in this setting may be obviated.

References

1. Gomori JM, Grossman RI, Goldberg HI, Zimmerman RA, Bilaniuk LT. **Intracranial hematomas: imaging by high-field MR.** *Radiology* 1985;157:87–93
2. Clark RA, Watanabe AT, Bradley WG, Roberts JD. **Acute hematomas: effects of deoxygenation, hematocrit, and fibrin-clot formation and retraction on T2 shortening.** *Radiology* 1990;175:201–206
3. Hayman A, Chin HY, Kirkpatrick JB, et al. **Temporal changes in RBC hydration: application to MR of blood.** In: *Proceedings of the Annual Meeting of the American Society of Neuroradiology, Los Angeles, 1990.* Oak Brook, IL: American Society of Neuroradiology; 1990:314
4. Edelman RR, Johnson K, Buxton R, et al. **MR of hemorrhage: a new approach.** *AJNR Am J Neuroradiol* 1986;7:751–756
5. Thulborn KR, Sorensen AG, Kowell NW, et al. **Biochemical correlation of the magnetic resonance appearance of experimentally induced cerebral hemorrhage in the rat.** *AJNR Am J Neuroradiol* 1990;11:291–297
6. Selden C, Peters TJ. **Separation and assay of iron proteins in needle biopsy specimens of human liver.** *Clin Chim Acta* 1979;98: 47–52
7. Vidnes A, Helgeland L. **Sex and age differences in the hemosiderin content of rat liver.** *Biochim Biophys Acta* 1973;328:365–372
8. Kreindler A, Marcovici G, Florescu I. **Histoenzymologic and biochemical investigations into the nervous tissue round an experimentally-induced cerebral hemorrhagic focus.** *Rev Roum Neurol* 1972;9:313–319
9. Lalonde JMA, Ghadially FN, Massey KL. **Ultrastructure of intramuscular haematomas and electron-probe X-ray analysis of extracellular and intracellular iron deposits.** *J Pathol* 1978;125:17–23
10. Gomori JM, Grossman RI, Yu-Ip C, Asakura T. **NMR relaxation times of blood: dependence on field strength, oxidation state, and cell integrity.** *J Comput Assist Tomogr* 1987;11:684–690
11. Atlas SW, Mark AS, Gomori JM, Grossman RI. **Intracranial hemorrhage: gradient echo imaging at 1.5 T: comparison with spin-echo imaging and clinical applications.** *Radiology* 1988;168:803–807
12. Barkovich AJ, Atlas SW. **Magnetic resonance imaging of intracranial hemorrhage.** *Radiol Clin North Am* 1988;26:801–820
13. Brooks RA, Di Chiro G, Patronas N. **MR imaging of cerebral hematomas at different field strengths: theory and applications.** *J Comput Assist Tomogr* 1989;13:194–206
14. Gomori JM, Grossman RI. **Head and neck hemorrhage.** In: Kressel HY, ed. *Magnetic Resonance Annual 1987.* New York: Raven Press; 1987:71–112
15. Grossman RI, Gomori JM, Goldberg HI, et al. **MR imaging of hemorrhage conditions of the head and neck.** *Radiographics* 1988; 8:441–454

16. Thulborn KR, Brady TJ. **Iron in magnetic resonance imaging of cerebral hemorrhage.** *Magn Reson Q* 1989;5:23–38
17. Thulborn KR, Atlas SW. **Intracranial hemorrhage.** In: Atlas SW, ed. *Magnetic Resonance Imaging of the Brain and Spine.* New York: Raven Press; 1991:175–224
18. Brooks RA, Brunetti A, Alger JR, Di Chiro G. **On the origin of paramagnetic inhomogeneity effects in blood.** *Magn Reson Med* 1989;12:241–248
19. Bryant RG, Marill K, Blackmore C, Francis C. **Magnetic relaxation in blood and blood clots.** *Magn Reson Med* 1990;13:133–144
20. Bydder GM, Pennock JM, Porteous R, Dubowitz LM, Gadian DG. **MRI of intracerebral hematoma at low field (0.15T) using T2 dependent partial saturation sequences.** *Neuroradiology* 1988;30: 367–371
21. DeLaPaz RL, New PFJ, Buonanno FS, et al. **NMR imaging of intracranial hemorrhage.** *J Comput Assist Tomogr* 1984;8:599–607
22. Di Chiro G, Brooks RA, Girton ME, et al. **Sequential MR studies of intracerebral hematomas in monkeys.** *AJNR Am J Neuroradiol* 1986;7:193–199
23. Hackney DB, Atlas SW, Grossman RI, et al. **Subacute intracranial hemorrhage: contribution of spin density to appearance on spin-echo MR images.** *Radiology* 1987;165:199–202
24. Sipponen JT, Sepponen RE, Sivula A. **Nuclear magnetic resonance (NMR) imaging of intracranial hemorrhage in the acute and resolving phases.** *J Comput Assist Tomogr* 1983;7:954–959
25. Thulborn KR, Waterton JC, Matthews PM, Radda GK. **Oxygenation dependence of the transverse relaxation time of water protons in whole blood at high field.** *Biochim Biophys Acta* 1982;714:265–270
26. Wismer GL, Buxton RB, Rosen BR, et al. **Susceptibility induced magnetic resonance line broadening: applications to brain iron mapping.** *J Comput Assist Tomogr* 1988;12:259–265
27. Zimmerman RD, Heier LA, Snow RB, Liu DPC, Kelly AB, Deck MDF. **Acute intracranial hemorrhage: intensity changes on sequential MR scans at 0.5T.** *AJNR Am J Neuroradiol* 1988;9:47–57
28. Weingarten K, Zimmerman RD, Deo-Narine V, Markisz J, Cahill PT, Deck MD. **MR imaging of acute intracranial hemorrhage: findings on sequential spin-echo and gradient-echo images in a dog model.** *AJNR Am J Neuroradiol* 1991;12:457–467
29. Gomori JM, Grossman RI, Asakura T, et al. **An in vitro study of magnetization transfer and relaxation rates of hematoma.** *AJNR Am J Neuroradiol* 1993;14:871–880
30. Yamada N, Imakita S, Nishimura T, Takamiya M, Naito H. **Evaluation of the susceptibility effect on gradient echo phase images in vivo: a sequential study of intracerebral hematoma.** *Magn Reson Imaging* 1992;10:559–571
31. Nath FP, Kelly PT, Jenkins A, Mendelow AD, Graham DI, Teasdale GM. **Effects of experimental intracerebral hemorrhage on blood flow, capillary permeability, and histochemistry.** *J Neurosurg* 1987;66:555–562